Microchimica Acta (2019) 186: 651
https://doi.org/10.1007/s00604-019-3752-7

ORIGINAL PAPER

Simultaneous voltammetric determination of acetaminophen, naproxen, and theophylline using an in-situ polymerized poly(acrylic acid) nanogel covalently grafted onto a carbon black/La_2O_3 composite

Bhuvanenthiran Mutharani[1] · Palraj Ranganathan[2,3] · Shen-Ming Chen[1] · Chelladurai Karuppiah[4]

Received: 17 April 2019 / Accepted: 10 August 2019 / Published online: 28 August 2019

Abstract

Lanthanum oxide nanomaterials were decorated with carbon black (CB) and grafted with a poly(acrylic acid) nanogel to obtain a composite material (CB-g-PAA/La_2O_3) for simultaneous determination of acetaminophen (AMP), naproxen (NPX), and theophylline (TPH). The nanogel was synthesized by in-situ free radical polymerization. The composite was dropped onto a glassy carbon electrode (GCE), and the modified GCE displays robust electrocatalytic activity towards AMP, NPX, and TPH, with voltammetric signals that are enhanced compared to a bare GCE. Features of merit for AMP, NPX, and TPH, respectively, include (a) peak potentials of 0.42, 0.85 and 0.12 V (vs. Ag/AgCl), (b) linear ranges from 0.05–887, 0.05–884, and 0.02–888 μM, and (c) detection limits of 20, 35, and 15 nM. The practical applicability of the CB-g-PAA/La_2O_3/GCE was illustrated by analyzing serum and urine samples.

Keywords Electroanalytical · Simultaneous determination · Nanogel · Human blood serum · And urine samples

Introduction

Acetaminophen, also known asparacetamol or tylenol, does not cause any noxious effects but an overindulge quantities (4.0 g/daily) gives rise to serious negative effects [1]. Curative concentration levels in plasma are 10–25 μg mL^{-1}, though, its toxicity concentration level is larger than 200 μg mL^{-1} [2]. Naproxen, [(S)-2-(6-methoxy-2-naphthyl) propanoic acid; NPX] is also an analgesic, antipyretic and anti-inflammatory drug and is a non-selective cyclooxygenase-2 inhibitor [3]. But, an overdose of NPX is causing severe upper gastrointestinal bleeding complications [4, 5], and hepatic toxicity [6], while its photoproducts were reported as eco-toxic [7]. Another important drug, theophylline, (1,3-dimethylxanthine; TPH) is a xanthine-based alkaloid, commonly utilized as a popular clinical drug for the treatment of respiratory diseases, which has been clinically used for more than 80 years [8]. Therapeutic accepted plasma levels of TPH concentration range in adults is of 5–20 μg mL^{-1}. High dosage level (over 20 μg mL^{-1}) in blood serum can cause permanent neurological damage and cardiac arrest [9]. As an outcome, it is immense prominent to constitute an effective method for the simultaneous determination of AMP, NPX, and TPH. Lately, electrochemical techniques are broadly applied and favored over other techniques owing to their significant advantages and important applications in the biochemical analysis [10].

Transition metal oxides have been widely reported as electrocatalysts both in theoretical calculations and

Electronic supplementary material The online version of this article (https://doi.org/10.1007/s00604-019-3752-7) contains supplementary material, which is available to authorized users.

✉ Shen-Ming Chen
smchen78@ms15.hinet.net

[1] Department of Chemical Engineering and Biotechnology, National Taipei University of Technology, No. 1, Section 3, Chung-Hsiao East Road, Taipei 106, Taiwan, Republic of China

[2] Institute of Organic and Polymeric Materials, National Taipei University of Technology, No. 1, Section 3, Chung-Hsiao East Road, Taipei 106, Taiwan, Republic of China

[3] Research and Development Center for Smart Textile Technology, National Taipei University of Technology, No. 1, Section 3, Chung-Hsiao East Road, Taipei 106, Taiwan, Republic of China

[4] Battery Research Center of Green Energy, Ming Chi University of Technology, New Taipei City 243, Taiwan, Republic of China

experimental synthesis owing to their promising and improving electrocatalytic activity [11]. Among all the transition metal oxides, lanthanum and its oxides (La_2O_3) have attracted significant interest (i.e. two oxidation states La^{2+} and La^{3+}, excellent redox activity and thermal stability). And also their intensive use in photo-catalysis, microelectronic, electrocatalysis, oxygen evaluation reaction, oxygen reduction reaction, and other applications [12]. For maximizing the electrocatalytic activity of La_2O_3 nanomaterials, a suitable carbon support material is needed for their dispersion [13].

Compared to conventional carbonaceous materials including graphene and carbon nanotubes, carbon black (CB) is an attractive and promising candidate because of their high surface area-to-volume ratios, low cost and a numerous number of defect sites [14]. Therefore, the combination of CB and La_2O_3 hybrid would interest material for potential electrocatalyst [15]. However, the weak interaction between metal nanoparticles (MNP) and CB causes the low dispersion and aggregation of MNP on CB. Consequently, decreases the active surface area, which leads to a poor electrocatalytic activity. The poor dispersion and agglomerating of CB, due to its strong hydrophobicity (π-π stacking of sp^2 carbon), are significant hurdles to practical implementation. Hence, it is prominent to discover a strategy for the synthesis of uniform distribution of La_2O_3 on CB support to enhance the stability and electrocatalytic activity. In this context, surface functionalization of CB using oxide modification is well established. Despite, in this modification method, the tips and defects of CB can be eliminated and easily cut short owing to the strong acidic condition [16–18]. Therefore, the covalent graft-functionalization of CB surface with polymer is much attractive because the polymer can avert the accumulation and upgrade the distribution of La_2O_3 nanomaterials on the surface of CB [19, 20]. Especially, the polyanion poly (acrylic acid) (PAA) is one of the fascinating polymers which can avert the restacking of CB. Additionally, a large number of carboxylic acid (COOH) groups in the PAA backbone chains can form coordination covalent bonds to metal oxides which can enhance the dispersion and avert the aggregation of La_2O_3 nanomaterials on CB support.

Considering the properties of functionalized polymer-carbon hybrid catalysts and its electrocatalytic applications [21], here, we constructed a carbon black grafted with poly(-acrylic acid) nanogel (CB-g-PAA) hybrid catalyst using in situ free radical polymerization method. Later, La_2O_3 nanomaterials were decorated on the surface of CB-g-PAA. The hybrid catalyst will have good film-forming properties based on PAA fragment. The aim of this study is to use CB-g-PAA/La_2O_3 hybrid catalyst for the simultaneous electrochemical determination of AMP, NPX, TPH drugs. The dispersed CB-g-PAA/La_2O_3 is simply dropping cast onto GCE surfaces after which the sensor is ready to be utilized. The results of the CB-g-PAA/La_2O_3/GCE provide desirable electrochemical movement to the simultaneous determination of AMP, NPX, and TPH. The suggested electrochemical sensing platform was successfully employed to detect the concentration of AMP, NPX, and TPH in human blood serum and urine samples.

Experimental section

Materials and methods

Carbon black (CB), acrylic acid (AA), $La(NO_3)_3$. $6H_2O$, ascorbic acid (AAD), 2,2′-azo-bis-(isobutyronitrile) (AIBN), acetaminophen (AMP), naproxen (NPX), theophylline (TPH), catechol (CC), resorcinol (RSC), hydroquinone (HQ), polyethylene glycol (PEG 20000), and chlorpromazine (CPZ) were acquired from Sigma Aldrich Co., Ltd. (https://www.sigmaaldrich.com/catalog/product). All other chemicals were acquired from a local chemical agent and the deionized (DI) water and 0.1 M phosphate buffer electrolyte by using both disodium hydrogen phosphate (Na_2HPO_4) and sodium dihydrogen phosphate (NaH_2PO_4). It was utilized throughout the experiments.

Instrumentation

The identification of functional groups on the La_2O_3 and CB-g-PAA/La_2O_3 was characterized by using CHI1600 Fourier transform infrared spectroscopy (FT-IR) instrument in the ranges of 450–4500 cm^{-1}. X-ray diffraction (XRD) patterns were acquired from the XPERT PRO instrument. Field emission scanning electron microscopy (FE-SEM) images were captured with a Hitachi J600F FE-SEM instrument. The oxidation states of CB-g-PAA/La_2O_3 were identified using Thermo ESCALAB 250 X-ray photoelectron spectroscopy (XPS) analyzer instrument. Differential pulse voltammetry (DPV) and cyclic voltammetry (CV) experiments were conducted utilizing CHI 1900 and CHI 1205 B electrochemical analyzer in a typical three-electrode cell system. A platinum wire (Pt) and Ag/AgCl (sat. KCl) as a reference and auxiliary electrodes, respectively. The CB-g-PAA/La_2O_3/GCE as working electrode. The electrochemical impedance spectroscopy (EIS) of different electrodes were conducted by using ZHAKNER Elektrik instrument.

Functionalization of carbon black (CB) with PAA nanogel

Polymer nanogel functionalized CB was synthesized through in situ free radical polymerization method, as shown in Scheme 1a. In a typical synthesis, 1 g of AA

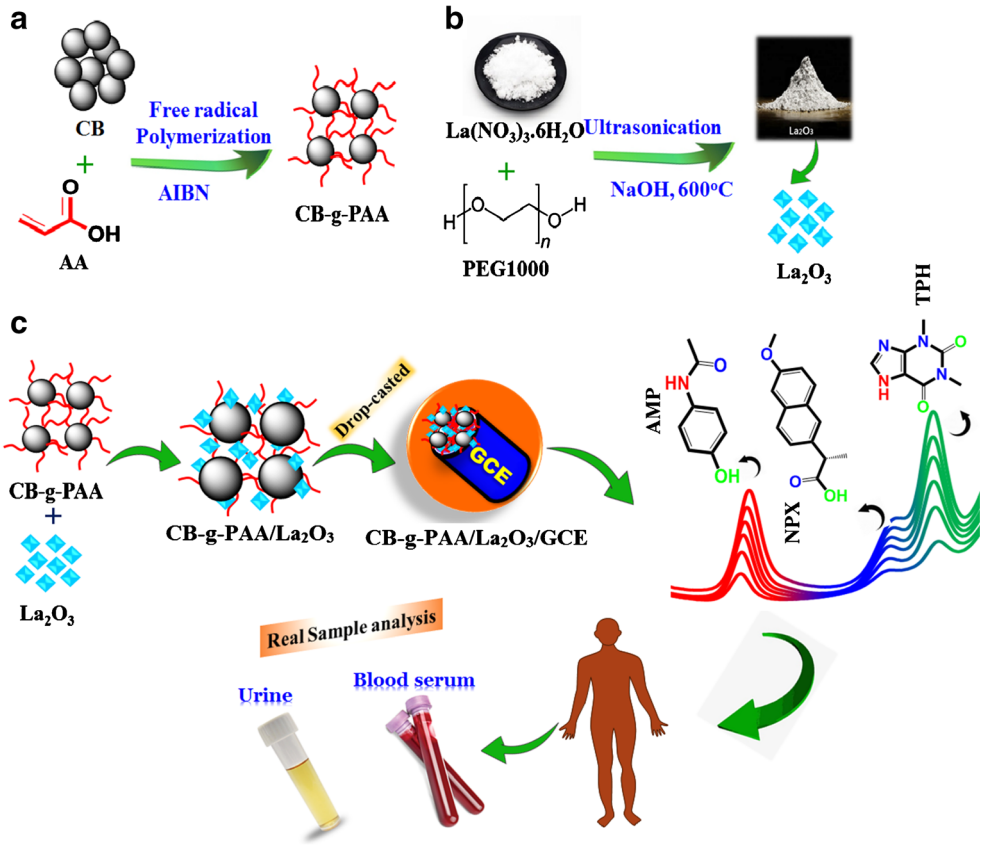

Scheme 1 Schematic illustration: (**a**) synthesis of CB-g-PAA. (**b**) Synthesis of La_2O_3. (**c**) The overall synthesis procedure of CB-g-PAA/La_2O_3 and its electrochemical oxidation of AMP, NPX, and TPH.

was added into a three-necked round-bottom reaction pitcher containing acetone (100 mL) and 0.1 g of CB. After ultra-sonication for 10 min, the solution was purged with nitrogen for 35 min to deoxygenation, followed by being the addition of 0.05 g of AIBN initiator. Further, the mixed solution was kept at 55 °C for 8 h. Finally, the poly(acrylic acid) nanogel grafted CB (CB-g-PAA) was dialyzed against the unreacted monomer for 24 h and washed with DI water 5 times to rid of physically adsorbed PAA nanogel from CB. PAA nanogel was formed by the same procedure in the absence of CB.

Preparation of La_2O_3 nanomaterials

La_2O_3 was synthesized via ultra-sonication method, as shown in Scheme 1b. Prior to the synthesis, 50 mg of $La(NO_3)_3.6H_2O$ and 0.25 g of PEG 20000 were added into the 25 mL of DI water and kept it for ultra-sonication at ambient temperature. Then, 75 mL of NaOH solution (5 mg) was added progressively into the above solution during the ultra-sonication. After finishing the ultra-sonication treatment for 2 h, the white precipitates were isolated through filtration, washed with DI water and ethanol several times to remove the other impurities. Finally, the product was dried and calcined at 700 °C for 3 h to afford the La_2O_3 catalyst.

Synthesis and fabrication of CB-g-PAA/La_2O_3 modified electrodes

CB-g-PAA/La_2O_3 hybrid catalyst was synthesized by the ultra-sonication process. About 10 mg of CB-g-PAA and 5 mg of La_2O_3 nanomaterials were mixed together with 1 mL of DI water and then ultrasonicated for 2 h to induce the formation of La_2O_3 nanomaterials on CB-g-PAA surface. Under the same condition, 10 mg of CB-g-PAA and 5 mg of La_2O_3 were separately mixed in each 1 mL of DI water and ultrasonicated until 1 h for the control experiment. Later, these catalysts were drop cast on the pre-cleaned GCE surface for further use. Prior to clean the GCE, it was polished well with 0.05 μm alumina powder using the polishing pad and rinsed with DI water thoroughly. About 6 μL of aforesaid catalysts were drop cast on the surface of GCE separately and dried in an oven at 40 °C and it was used for the evaluation of all electrochemical experiments. Scheme 1c shows the overall synthesis procedure with a schematic illustration of CB-g-PAA/La_2O_3 and its simultaneous electrochemical determination of AMP, NPX, and TPH.

Choice of materials

Nowadays, the various carbonaceous materials including reduced graphene oxide and carbon dots, carbon nanotubes.

Carbon black (CB) is an effective and promising candidate owing to their high surface area-to-volume ratios, low cost and a numerous number of defect sites and high conductivity. Nowadays, the various metal nanoparticles, oxides, and sulfides (AuNPs; ZnO; MoS_2) are widely used as an electrocatalyst due to the high surface area. Among, the metal oxide such as La_2O_3 has surface defects and oxygen vacancies help to improve the electrocatalytic activity. Although, the combination of CB and La_2O_3 can be an attractive material for potential electrocatalyst, and also it leads to decreases the electrocatalytic activity owing to its low dispersion. Among the various polymers such as PPy, PANI, we selected the PAA-functionalization CB with La_2O_3 hybrid for the simultaneous determination of AMP, NPX, and TPH, because of their dispersion ability, high conductivity leads to the higher electrocatalytic activity.

Results and discussion

Characterization of the CB-g-PAA/La_2O_3

Fig. S1A shows FT-IR spectra of CB, CB-g-PAA, La_2O_3 and CB-g-PAA/La_2O_3. The virgin CB had characteristic peaks at 3434 cm^{-1} (V_{O-H}), 1629 cm^{-1} ($V_{C=C}$) (Fig. S1A (a)). After PAA was grafted on CB surface (Fig. S1A (b)), a new peak appears at 3009 cm^{-1} (V_{O-H}), 1703 cm^{-1} (V_{COOH}), and 1574 cm^{-1} ($V_{sodiun\ carboxyl\ anion}$) which is the characteristic peaks of PAA. These results indicated that PAA was successfully grafted onto the CB surface. La_2O_3 nanomaterials had a characteristic peak at 467 and 652 cm^{-1} (V_{La-O}) (Fig. S1A (c)), whereas, after the formation of La_2O_3 nanomaterials on CB-g-PAA surface, all of the characteristic absorbance peaks of CB-g-PAA and La_2O_3 obviously appear. These results indicate that CB-g-PAA/La_2O_3 was formed successfully. However, compared to CB-g-PAA (Fig. S1A (b)), V_{COOH} peak at 1703 cm^{-1} is split into an asymmetric ($V_{as\ COO-}$) and symmetric ($V_{s\ COO-}$), stretch band at, respectively, 1593 cm^{-1} and 1698 cm^{-1} (Fig. S1A (d)). This result proves that the formation of a coordination chemical bond between the La_2O_3 surface and the PAA carboxylic group [22]. There are three potential coordination modes for attachment of a carboxylate group of PAA to a La_2O_3 surface including monodentate, chelating and bridging bidentate [23]. Fig. S1B shows the schematic of this mechanism.

To evidently identify the La_2O_3 and La_2O_3 hybrid structure, the samples were scrutinized by XRD, as shown in Fig. S2. For all samples, the diffraction peak assigned to about 26° is attributed to the amorphous structure of CB. The diffraction peaks at 26.3°, 29.4°, 39.8°, 46.8°, 52.3°, 55.5°, 56.8°, 60.7°, and 63.4° can be ascribed to the hexagonal phase of La_2O_3 (JCPDS card 05–0602). No other peaks can be observed. This confirms the hexagonal structure of the La_2O_3 in the hybrid catalyst.

To study the surface morphology of our hybrid catalyst, we have performed an FE-SEM analysis. From Fig. 1a, pristine CB have relatively cotton-seed like spheres structure. After the free radical graft polymerization of PAA, CB is covered with a thin layer of PAA polymer (Fig. 1b), indicating the successful grafting of PAA on the surface of CB. Figure 1c shows the microstructure of virgin La_2O_3 nanomaterials and the particles are agglomerated. From Fig. 1d, it can be clearly seen that the case of the preparation of the La_2O_3 with PAA (CB-g-PAA/La_2O_3), La_2O_3 nanomaterials were homogeneously distributed on CB surface due to the covalent bonding of PAA with La_2O_3. This leads to the increase of effective active sites. Further, we also investigated the energy-dispersive X-ray spectroscopy (EDS) and elemental mapping images to confirm the formation of CB-g-PAA/La_2O_3 and is shown in Fig. S3A-C, and Fig. S4A-D.

XPS is an efficient technique that can provide information on oxidation states and elemental analysis of CB-g-PAA/La_2O_3. As shown in Fig. 2a, the overall XPS survey spectrum of CB-g-PAA /La_2O_3, which indicates the presence of all elements (carbon (C), oxygen (O) and lanthanum (La)) in CB-g-PAA/La_2O_3. The high-resolution C 1 s core-level spectra in Fig. 2b exhibits four binding energies at 284.9 eV, 285.5 eV, 288.5 eV and 293 eV due to the presence of C-OH, C-O-C, C-O and COOH groups in CB-g-PAA [24]. The high-resolution spectrum of O 1 s (532.1 eV and 534.5 eV) confirms the existence of La-O and adsorbed oxygen species at CB-g-PAA/La_2O_3 (Fig. 2c). With regard to La 3d (Fig. 2d), the binding energies are located at 838.2 eV and 855 eV along with the shake-up peaks at 842.1 eV and 858.3 eV assigned to La $3d_{5/2}$ and La $3d_{3/2}$, respectively [25].

Electrochemical characterization of modified electrodes

The electron transfer kinetics of redox probes at the CB-g-PAA/La_2O_3/GCE was demonstrated with EIS. Fig. S5A shows the corresponding Nyquist plots of bare GCE (i), La_2O_3/GCE (ii), CB-g-PAA/GCE (iii) and CB-g-PAA/La_2O_3/GCE (iv) in 5 mM $[Fe(CN)_6]^{3-/4-}$ containing 0.5 M KCl at the frequency range of 100 MHz-1 kHz. Upper left inset in Fig. S5A illustrates the Randles circuit model to fit the impedance curve. The electron transfer resistance (R_{ct}) value for the $[Fe(CN)_6]^{3-/4-}$ was calculated as the semicircle diameter of the high-frequency region at Nyquist plots. The R_{ct} value of about 528 Ω is observed for GCE due to the sluggish electron transfer kinetics and electro-inactive species on the surface of bare GCE. Whereas, the R_{ct} of GCE modified by La_2O_3 and CB-g-PAA is of 430 Ω and 248 Ω, respectively, which is due to the high redox-active and conductive carbon materials modified on the GCE. However, their R_{ct} is still high

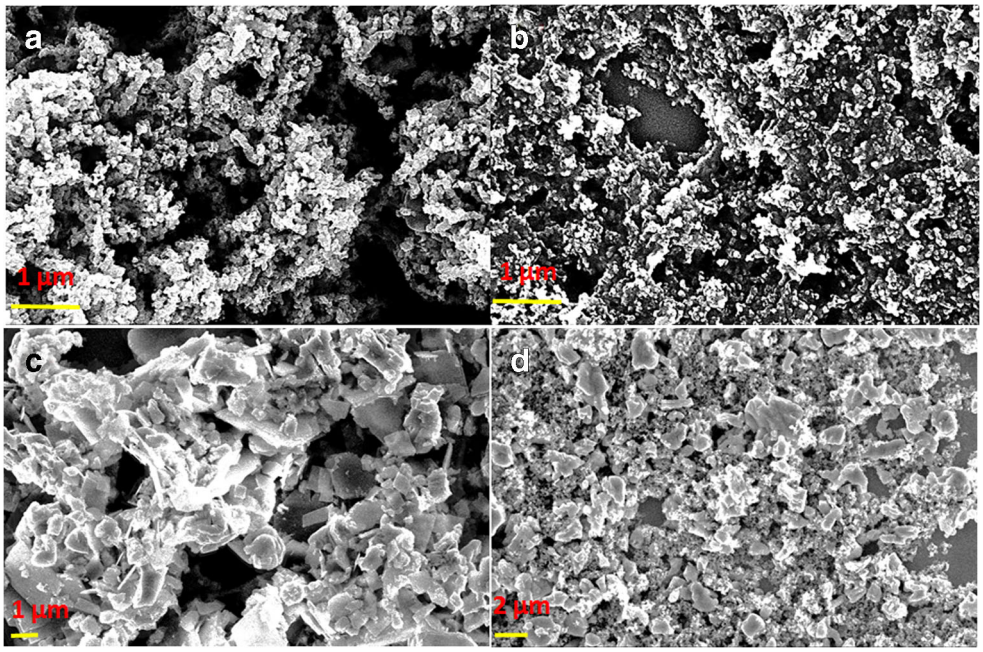

Fig. 1 FE-SEM images of (**a**) CB, (**b**) CB-g-PAA, (**c**) La_2O_3, (**d**) CB-g-PAA/La_2O_3 of (**b**) C 1 s, (**c**) O 1 s and (**d**) La 3d

owing to the more oxygen functionality that can strictly restrict the oxygen transport to the GCE surface. On the other hand, the R_{ct} value was completely reduced when GCE modified by CB-g-PAA/La_2O_3 (97 Ω), owing to the coordination chemical bond between the La_2O_3 and the carboxylic group of PAA. The oxygen functionality on CB-g-PAA/La_2O_3 catalyst is significantly reduced which is clearly confirmed from the FT-IR analysis. Therefore, the electron transfer kinetics of CB-g-PAA/La_2O_3/GCE is increased.

Further, the electrochemical properties of bare GCE (i), La_2O_3/GCE (ii), CB-g-PAA/GCE (iii) and CB-g-PAA/La_2O_3/GCE (iv) was also examined by CV with 5 mM

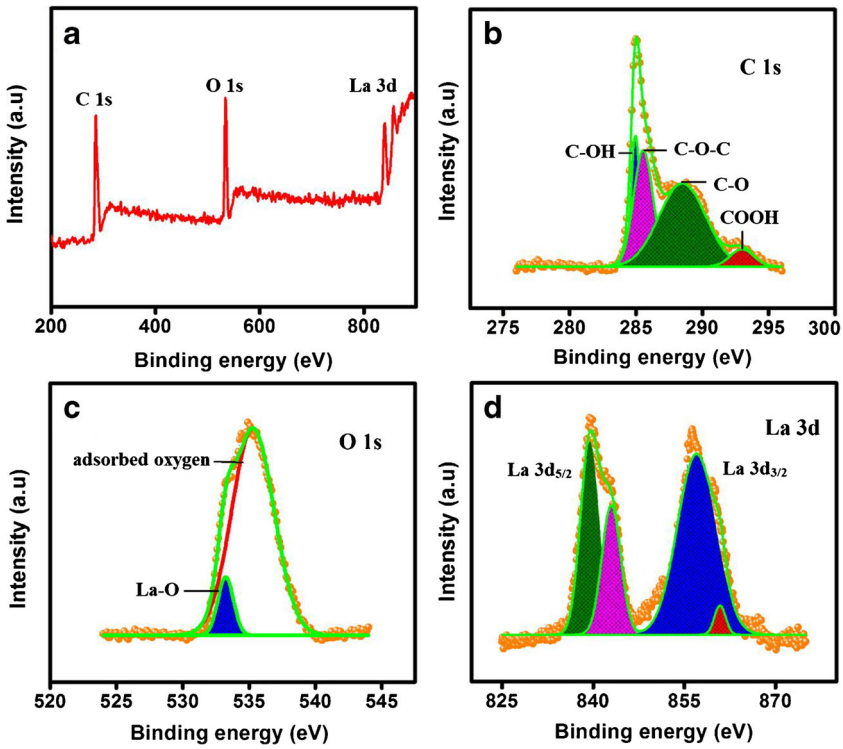

Fig. 2 **a** The overall XPS spectrum of CB-g-PAA/La_2O_3, high-resolution XPS spectroscopy

$[Fe(CN)_6]^{3-/4-}$ redox probe in 0.5 M KCl and is depicted in Fig. S5B. A pair of weak redox peaks were observed at bare GCE, which suggest that the sluggish electron transfer at the interface. While at La_2O_3/GCE, CB-g-PAA/GCE showed a well-defined redox peaks with a lower peak to peak separation compared to bare GCE. The modification of GCE with CB-g-PAA/La_2O_3 elevates the redox peak currents and decreases the difference in potential between the redox peaks due to its large effective active surface area. The surface area was calculated from the oxidation peak current (I_{pa}) based on the Randles Sevcik equation [Eq. 1],

$$I_{pa} = \left(2.65 \text{ x } 10^5\right) n^{3/2} A D^{1/2} C v^{1/2} \quad (1)$$

where I_{pa} is the anodic peak current, n is the number of electrons participated in the reaction, A is the electroactive surface area, D is the diffusion coefficient, C is the concentration and v is the scan rate. The electro active surface area values were found to be 0.089 cm^2, 0.075 cm^2, 0.051 cm^2, and 0.036 cm^2 for CB-g-PAA/La_2O_3/GCE, CB-g-PAA/GCE, La_2O_3/GCE, and bare GCE (0.036 cm^2). These result implies that the higher active surface area can effectively decrease the peak-to-peak separation and increase fast electron transport. Fig. S5C illustrates the CV of CB-g-PAA/La_2O_3/GCE in 5 mM $[Fe(CN)_6]^{3-/4-}$ containing 0.5 M KCl at different scan rates were ranging from 10 to 100 mV s^{-1}. The redox peak currents were linearly plotted against as a function of the square root of scan rate and the corresponding results are shown in Fig. S5D.

Electrochemical behaviors of acetaminophen, naproxen, and theophylline (AMP, NPX, and TPH)

The electrochemical sensing properties of bare GCE (ii), La_2O_3/GCE (iii), CB-g-PAA/GCE (iv), and CB-g-PAA/La_2O_3/GCE (v) were demonstrated by CV to detect 200 μM AMP, NPX, and TPH (0.1 M phosphate buffer) simultaneously and absence (i) of three analytes at 50 mV s^{-1} (Fig. 3a). For bare GCE, broad oxidation peaks are observed for AMP, NPX, and TPH, which indicates that the poor electron transfer property of bare GCE and it lacks the ability to distinguish those analytes. Whereas, the La_2O_3/GCE shows the higher oxidation peak current and negative potential shift than the bare GCE, however, three oxidation peaks are not clearly separated by La_2O_3/GCE. It is due to the high resistance of the electrode surface. As compared to bare GCE and La_2O_3/GCE, the CB-g-PAA/GCE were exhibited higher oxidation peaks well clear peak separation for AMP, NPX, and TPH. On the other hand, the electrocatalytic activity towards these analytes is enhanced at CB-g-PAA/La_2O_3/GCE, where the three distinct, non-interfering, well-separated and higher anodic peaks are observed for AMP, NPX, and TPH. A pair of well-defined redox peaks of AMP was observed at E_{pa} = 0.42 V and E_{pc} = 0.25 V corresponding to the oxidation of the hydroxyl group to a carbonyl group (N-acetyl-p-benzoquinone imine) in the benzene ring of AMP. And also the reversible reduction from the carbonyl group (N-acetyl-p-benzoquinone imine) to AMP on the CB-g-PAA/La_2O_3/GCE with two electrons and two protons electrochemical process [26]. The oxidation peak of NPX at E_{pa} = 0.85 V due to the oxidation of the hydroxyl group to radical with involving one electron and one proton transfer process [27]. The anodic peak of TPH is located at E_{pa} = 1.02 V due to the oxidized form of TPH [28].

On the basis of the CV results, we concluded that CB-g-PAA/La_2O_3 can interact with AMP, NPX, and TPH through three kinds of interactions: (1) hydrophilic region of PAA on CB act as an excellent stabilizing and dispersing agent for the La_2O_3 on the surface of CB-g-PAA due to the coordination covalent bond. This can deter the aggregation and improve the dispersion of La_2O_3 on CB-g-PAA surface, which lead to enhance the active surface area and consequently improve the electrocatalytic activity. (2) the large π conjugated structure of CB can form π-π stacking interaction with the aromatic group of the AMP, NPX, and TPH.

(3) H-bonding like the interaction between the hydroxyl and amide hydrogen of target drugs with the carboxyl group of PAA. This kind of interconnection network between the CB-g-PAA/La_2O_3 matrix and the AMP, NPX, and TPH analytes will be favorable for the direct electro-oxidation.

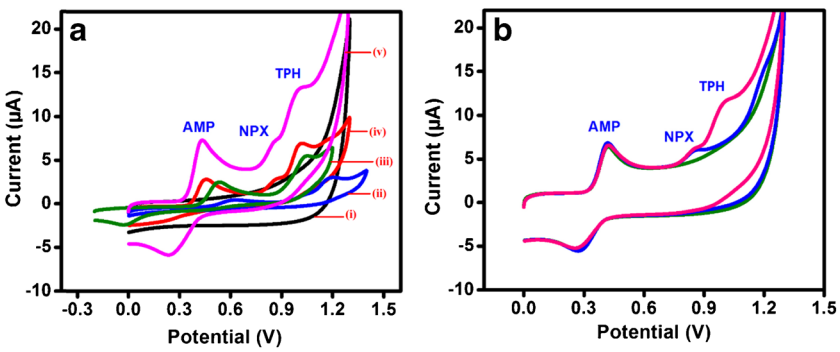

Fig. 3 **a** CV of simultaneous determination of three analytes at bare GCE (ii), La_2O_3/GCE (iii), CB-g-PAA/GCE (iv) and CB-g-PAA/La_2O_3/GCE (v) in 0.1 M phosphate buffer containing 200 μM AMP, NPX and TPH and absence (i) of 200 μM AMP, NPX, TPH at 50 mV s^{-1}. **b** The CV of each addition of 200 μM AMP (0.42 V), NPX (0.85 V), and TPH (0.1 V) at CB-g-PAA/La_2O_3/GCE in 0.1 M phosphate buffer at 50 mV s^{-1}

The plausible electro-oxidation mechanism of AMP, NPX, and TPH is illustrated in Scheme S1. Figure 3b shows each addition of 200 μM AMP, NPX, and TPH at CB-g-PAA/La_2O_3/GCE in 0.1 M phosphate buffer at 50 mV s^{-1}.

To further confirm the electrocatalytic activity of CB-g-PAA/La_2O_3/GCE toward AMP, NPX and TPH oxidation, the individual CV were monitored in different AMP, NPX and TPH concentrations range from 0 to 200 μM at 50 mV s^{-1}, as shown in Fig. 4a, c, and e. The redox currents of AMP and oxidation current of NPX and TPH increased linearly upon adding the different amounts of AMP, NPX and TPH (Fig. 4b, d, and f). This illustrates the excellent electrocatalytic activity of CB-g-PAA/La_2O_3/GCE. It is clearly seen that the well-separated signals for three compounds at CB-g-PAA/La_2O_3/GCE have more pertinent for the individual, and simultaneous determination. The influence of scan rate and pH studies are discussed briefly in ESM and is shown in Fig. S6- Fig. S9.

Simultaneous determination of acetaminophen, naproxen, and theophylline (AMP, NPX, and TPH)

The simultaneous determination of AMP, NPX, and TPH at CB-g-PAA/La_2O_3/GCE in 0.1 M phosphate buffer was explored by DPV in their mixture. When one analyte raised its concentration in the existence of the other two analytes, there is only one anodic peak current increased without interfering each other. As can be seen in Fig. 5a, the anodic peak currents (I_{pa}) of AMP increases linearly with increasing the concentration of 0.05–887 μM with the existence of 70 μM NPX, and TPH. The linear regression equation can be calibrated as I_{pa} (μA) = 0.0127 C_{AMP} + 0.9679; R^2 = 0.9983 for AMP (Fig. 5b). Figure 5c shows the linear increment in the anodic peak currents of NPX with varying the concentration ranges of 0.05–884 μM (in the presence of 40 μM AMP and TPH). The corresponding linear regression equation was expressed to be I_{pa} (μA) = 0.0119 C_{NPX} + 1.628; R^2 = 0.9955 for NPX

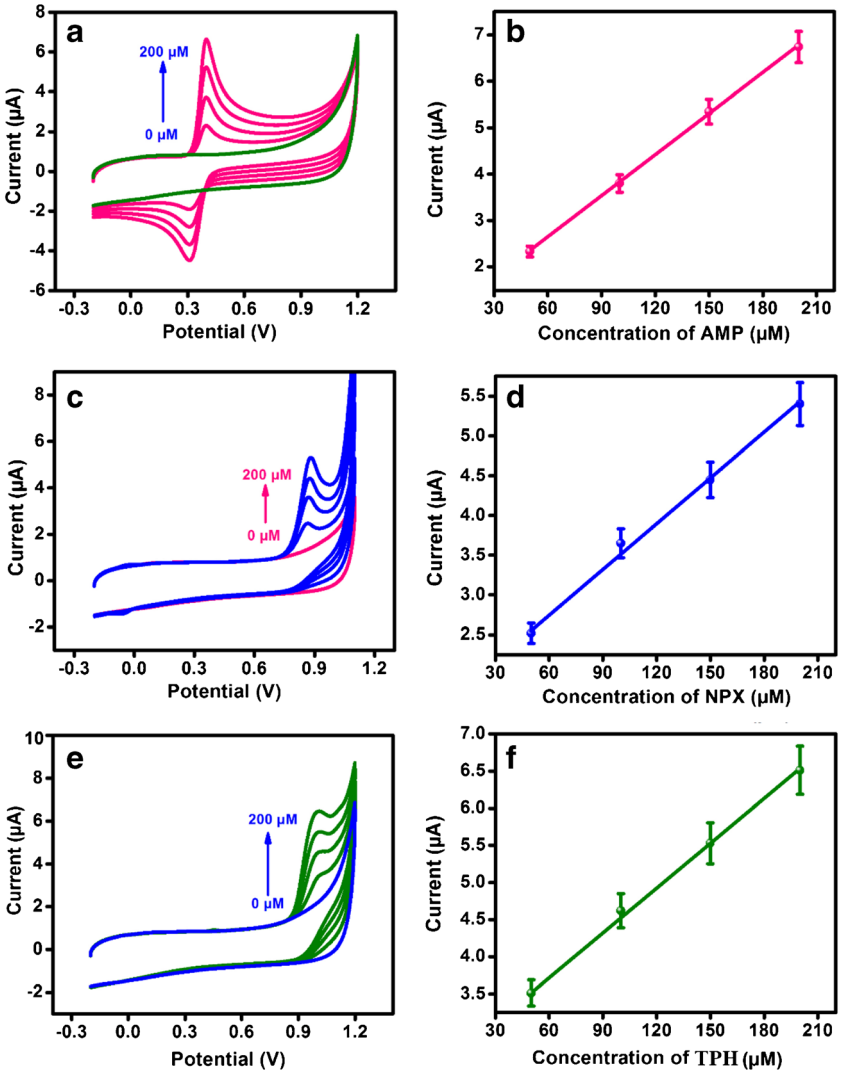

Fig. 4 CV scans of (A) AMP, (C) NPX, and (E) TPH on CB-g-PAA/La_2O_3/GCE in 0.1 M phosphate buffer (pH 7) with different concentration between 0 and 200 μM at 50 mV s^{-1} (n = 3). (B, D, and F) The corresponding linear plots of peak current vs. concentration (working potential = 0.42 V (AMP), 0.85 V (NPX), and 1.02 V (TPH))

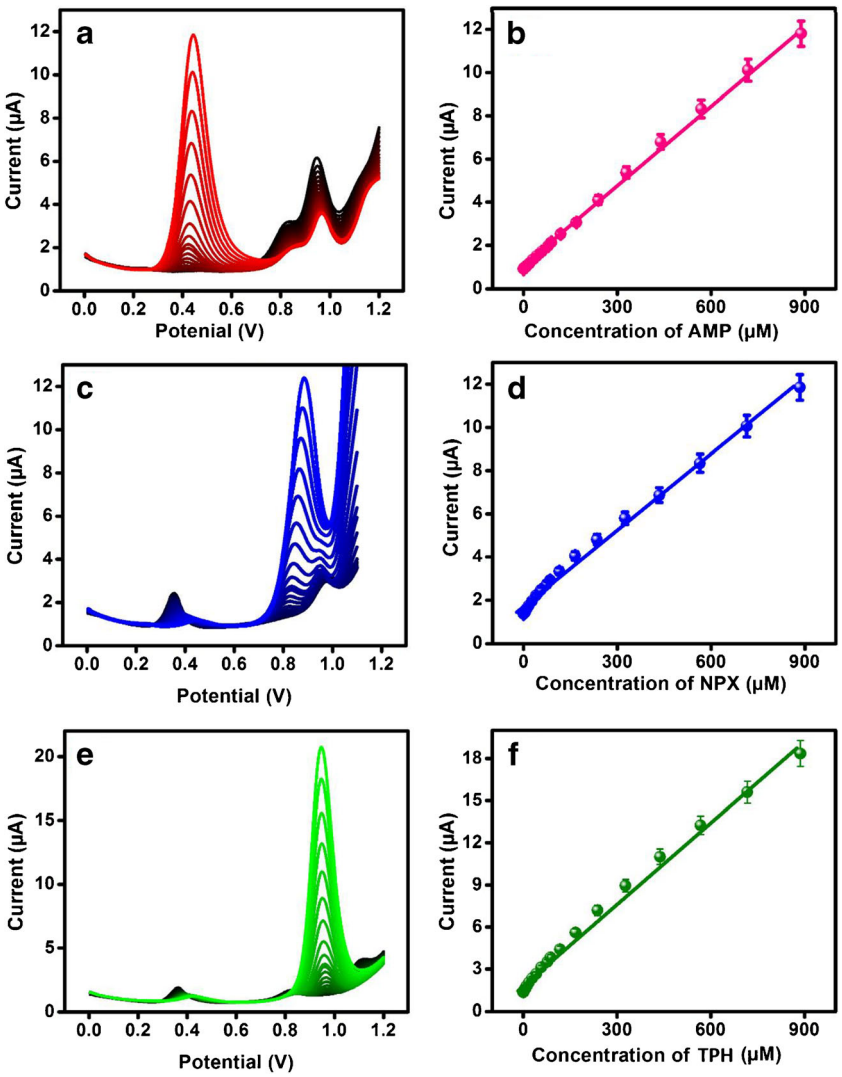

Fig. 5 DPV response of CB-g-PAA/La_2O_3/GCE (50 mV s^{-1}) with 0.1 M phosphate buffer (pH 7) containing (**a**) 70 μM each of NPX and TPH with different concentrations of AMP (0.05–887 μM) ($n = 3$). **c** 40 μM AMP and TPH with different concentrations of NPX (0.05–884 μM) (n = 3). **e** 30 μM AMP and NPX with different concentrations of TPH (0.02–888 μM) (n = 3). (B, D and F) The typical calibration plots of AMP, NPX, and TPH

(Fig. 5d). As shown in Fig. 5e, the anodic peak currents of TPH escalating linearly with increasing the different concentration were ranging from 0.02–888 μM (presence of 30 μM AMP and NPX).

In addition, the linear regression equation can be calculated as I_{pa} (μA) = 0.0188 C_{TP} + 1.8763; $R^2 = 0.9913$ for TP (Fig. 5f). The detection limit (LOD) of AMP, NPX, and TPH was calculated to be 20 nM, 35 nM, and 15 nM and the sensitivity of AMP, NPX, and TPH was found to be 2.21, 2.14, and 1.83 μA μM^{-1} cm^{-2}, respectively. The comparison of the analytical parameters of AMP, NPX, and TPH at CB-g-PAA/La_2O_3/GCE with other modified electrodes which previously reported articles are depicted in Table 1. As can be seen in Fig. S10A, the anodic peak currents of AMP, NPX, and TPH were escalating simultaneously with increasing the concentration from 20 to 120 μM. The linear regression coefficient of I_{pa} (μA) = 0.0276 C_{AMP} + 1.7453; $R^2 = 0.997$, I_{pa} (μA) = 0.0176 C_{NPX} + 1.996; $R^2 = 0.985$ and I_{pa} (μA) = 0.0434 C_{TP} + 2.674; $R^2 = 0.997$ for AMP, NPX, and TPH (Fig. S10B). It can be clearly seen that the CB-g-PAA/La_2O_3/GCE possesses the enhanced capability for the simultaneous determination of AMP, NPX, and TPH.

Stability, reproducibility and interference studies

To determine the stability of CB-g-PAA/La_2O_3/GCE, the DPV was conducted in 0.1 M phosphate buffer containing 50 μM AMP, NPX, and TPH (35 consecutive cycles) at 50 mV s^{-1} (Fig. S11A). After 35 successive cycles, the anodic current response of AMP, NPX, and TPH only reduced to 95%, which illustrates the good stability of CB-g-PAA/La_2O_3/GCE.

To determine the reproducibility of the CB-g-PAA/La_2O_3/GCE towards simultaneous detection of AMP, NPX, and TPH, the electrode was used to evaluate the solution containing 50 μM AMP, NPX, and TPH for 5 consecutive measurements. The relative standard deviations are found to be 1.63%, 3.51% and 2.61% for AMP, NPX, and TPH, illustrating the good reproducibility of CB-g-PAA/La_2O_3/GCE. To study the

Table 1 Comparisons of the CB-g-PAA/La_2O_3/GCE with Previous Reported Electrochemical Determinations of AMP, NPX, and TPH

Electrode type	linear range (μM)	Detection limit (μM)	Ref.
Thionine immobilized	0.1–100	0.05	[29]
EGR,ZnO/GCE	0.02–10	33	[30]
GCE	4–100	0.369	[31]
TiO2-GR/GCE	1–100	0.21	[32]
Au and glutamic acid/CPE	0.05–70	–	[33]
CB-g-PAA/La2O3/GCE	0.05–887	20 nM	This work(AMP)
Platinum electrode	1–25	0.24	[34]
ZnO/MWCNTs/CPE	1–200	0.23	[35]
MWCNT-Gr-IL/CCE	1–100	0.125	[27]
MWCNT/msCYP1A2-SPE	9–300	16	[36]
MWCNT/GCEs	10–100	0.6	[37]
CB-g-PAA/La_2O_3/GCE	0.05–884	35 nM	This work (NPX)
MWCNT/AuNP/PLL/SPE	10–200	2	[38]
MnO2-IL-Gr/GCE	01–10	0.1	[39]
AuNP-MWCNT0.25/GCE	0.5–20	0.09	[40]
CB-g-PAA/La2O3/GCE	0.02–888	15 nM	This work (TPH)

selectivity of CB-g-PAA/La_2O_3/GCE, several possible interferential species such as ascorbic acid (AAD), chlorpromazine (CPZ), resorcinol (RSC) hydroquinone (HQ), catechol (CC), dopamine (DA), and uric acid (UA) were investigated by DPV. It can be seen that the existence of a 50-fold excess concentration of aforesaid species such as AAD, CPZ, HQ, RSC, CC, DA, and UA exhibited negligible interferences (current response <5%) towards the simultaneous determination of 40 μM AMP, NPX, and TPH (Fig. S11B). This indicated an excellent selectivity of CB-g-PAA/La_2O_3/GCE.

Analysis of real samples

To confirm the applicability of a CB-g-PAA/La_2O_3/GCE sensor, the recovery results for the determination of AMP, NPX,

Table 2 Recovery test of the real samples

Sample	Added (μM)	Found (μM)	Recovery (%)	RSD (%)
		AMP		
Human blood serum	–	–	–	
	10	09.75	97.5	2.35
	15	14.50	96.6	3.55
	20	19.80	99.0	2.16
Urine	–	–	–	
	10	09.80	98.0	2.82
	15	14.25	95.0	2.44
	20	18.80	94.0	3.29
		NPX		
Human blood serum	–	–	–	
	10	09.85	98.5	2.62
	15	14.90	99.3	3.29
	20	19.90	99.5	2.94
Urine	–	–	–	
	10	09.70	97.0	2.05
	15	15.00	100.0	2.49
	20	19.00	95.0	3.39
		TPH		
Human blood serum	–	–	–	
	10	09.85	98.5	2.35
	15	14.75	98.3	3.36
	20	20.00	100.0	2.14
Urine	–	–	–	
	10	10.00	100.0	2.32
	15	14.99	99.3	3.23
	20	19.10	95.5	2.11

and TPH in human blood serum and urine samples were investigated by DPV (Fig. S12A-F). Before DPV determination, the 5 mL of human blood serum and urine samples were diluted 20 times with 0.1 M phosphate buffer and directly added to the 10 mL electrochemical cell containing phosphate buffer pH. There is no characteristic current response of AMP, NPX, and TPH when we added. Thus, the known concentration of AMP, NPX, and TPH was taken for the analysis.

The concentrations of AMP, NPX, and TPH were measured by the standard addition method. The corresponding recovery results were summarized in Table 2. The recovery results indicated that the CB-g-PAA/La_2O_3/GCE electrochemical sensing platform held great promise for reliable and sensing application in human blood serum and urine samples analysis.

Conclusions

We describe the fabrication of modified electrode with ultrasonication treated of La_2O_3 particles on CB-g-PAA hybrid catalyst for the effective simultaneous voltammetric determination of AMP, NPX, and TPH. The CV and DPV scans of the sensor exhibited three distinct peaks ascribed to oxidation of AMP, NPX, and TPH without interfering each other. Excellent electrochemical parameters of the CB-g-PAA/La_2O_3/GCE are compared with formerly reported literature owing to its conductivity, reactive sites, and the fast electron transport. Due to the formation of the coordinate covalent bond, which can lead to a high surface area with a remarkable decrease in overpotential and improved electrochemical performance of AMP, NPX, and TPH drugs. The CB-g-PAA/La_2O_3/GCE described the analytical utility for the qualitative and quantitative estimation of target drugs in human blood serum and urine samples with satisfactory results.

Acknowledgements This project was supported by the Ministry of Science and Technology (MOST 106-2113-M-027-003), Taiwan, ROC.

Compliance with ethical standards The author(s) declare that they have no competing interests.

References

1. Zhang Y, Huang Z, Wang L, Wang C, Zhang C, Wiese T, Wang G, Riley K, Wang Z (2018) Point-of-care determination of acetaminophen levels with multi-hydrogen bond manipulated single-molecule recognition (eMuHSiR). Anal Chem 90:4733–4740
2. Nourjah P, Ahmad SR, Karwoski C, Willy M (2006) Estimates of acetaminophen (paracetomal)-associated overdoses in the United States. Pharmacoepidemiol Drug Saf 15:398–405
3. Gouda AA, El-Sayed MIK, Amin AS, El Sheikh R (2013) Spectrophotometric and spectrofluorometric methods for the determination of non-steroidal anti-inflammatory drugs: a review. Arab J Chem 6:145–163
4. Bjarnason I, Thjodleifsson B (1999) Gastrointestinal toxicity of non-steroidal anti-inflammatory drugs: the effect of nimesulide compared with naproxen on the human gastrointestinal tract. Rheumatology (Oxford, England) 38:24–32
5. Giraud MN, Motta C, Romero JJ, Bommelaer G, Lichtenberger LM (1999) Interaction of indomethacin and naproxen with gastric surface-active phospholipids: a possible mechanism for the gastric toxicity of nonsteroidal anti-inflammatory drugs (NSAIDs)∗. Biochem Pharmacol 57:247–254
6. Victorino RM, Silveira JC, Baptista A, De Moura MC (1980) Jaundice associated with naproxen. Postgrad Med J 56:368–370
7. Isidori M, Lavorgna M, Nardelli A, Parrella A, Previtera L, Rubino M (2005) Ecotoxicity of naproxen and its phototransformation products. Sci Total Environ 348:93–101
8. Sullivan P, Jaffar Z, Page C, Costello J, Bekir S, Jeffery P (1994) Anti-inflammatory effects of low-dose oral theophylline in atopic asthma. Lancet. 343:1006–1008
9. Minton NA, Henry JA (1996) Treatment of theophylline overdose. Am J Emerg Med 14:606–612
10. Norouzi P, Haji-Hashemi H, Larijani B, Aghazadeh M, Pourbasheer E, Ganjali RM (2017) Application of new advanced electrochemical methods combine with nano-based materials sensor in drugs analysis. Curr Anal Chem 13:70–80
11. Zhang X, Xiao Q, Zhang Y, Jiang X, Yang Z, Xue Y, Sun K (2014) La_2O_3 doped carbonaceous microspheres: a novel bifunctional electrocatalyst for oxygen reduction and evolution reactions with ultrahigh mass activity. J Phys Chem C 118:20229–20237
12. Miah M, Bhattacharya S, Dinda D, Saha SK (2018) Temperature dependent supercapacitive performance in La_2O_3 nano sheet decorated reduce graphene oxide. Electrochim Acta 260:449–458
13. Ye W, Yu J, Zhou Y, Gao D, Wang D, Wang C, Xue D (2016) Green synthesis of Pt–Au dendrimer-like nanoparticles supported on polydopamine-functionalized graphene and their high performance toward 4-nitrophenol reduction. Appl Catal B 181:371–378
14. Silva TA, Moraes FC, Janegitz BC, Fatibello-Filho O (2017) Electrochemical biosensors based on nanostructured carbon black: a review. J Nanomater 2017:4571614
15. Gu W, Liu J, Hu M, Wang F, Song Y (2015) $La_2O_2CO_3$ encapsulated La_2O_3 nanoparticles supported on carbon as superior electrocatalysts for oxygen reduction reaction. ACS Appl Mater Interfaces 7:26914–26922
16. Jaffe A, Saldivar Valdes A, Karunadasa HI (2015) Quinone-functionalized carbon black cathodes for lithium batteries with high power densities. Chem Mater 27:3568–3571
17. Jiang Q, Wang S, Xu S (2018) Preparation and characterization of water-dispersible carbon black grafted with polyacrylic acid by high-energy electron beam irradiation. J Mater Sci 53:6106–6115
18. Tsubokawa N (1992) Functionalization of carbon black by surface grafting of polymers. Prog Polym Sci 17:417–470
19. Rubio N, Au H, Leese HS, Hu S, Clancy AJ, Shaffer MS (2017) Grafting from versus grafting to approaches for the functionalization of graphene nanoplatelets with poly (methyl methacrylate). Macromolecules 50:7070–7079
20. Zhou G, Xu X, Wang S, He X, He W, Su X, Wong CP (2017) Surface grafting of epoxy polymer on CB to improve its dispersion to be the filler of resistive ink for PCB. Results Phys 7:1870–1877
21. Tamaki T, Ito T, Yamaguchi T (2007) Immobilization of hydroquinone through a spacer to polymer grafted on carbon black for a high-surface-area biofuel cell electrode. J Phys Chem B 111: 10312–10319
22. Pedersen H, Söderlind F, Petoral RM Jr, Uvdal K, Käll PO, Ojamäe L (2005) Surface interactions between Y_2O_3 nanocrystals and organic molecules—an experimental and quantum-chemical study. Surf Sci 592:124–140

23. Madaeni SS, Zinadini S, Vatanpour V (2011) A new approach to improve antifouling property of PVDF membrane using in situ polymerization of PAA functionalized TiO_2 nanoparticles. J Membr Sci 380:155–162
24. Jiang Q, Wang S, Xu S (2018) Preparation and characterization of water-dispersible carbon black grafted with polyacrylic acid by high-energy electron beam irradiation. J Mater Sci 53:6106–6115
25. Chen S, Pan B, Zeng L, Luo S, Wang X, Su W (2017) $La_2Sn_2O_7$ enhanced photocatalytic CO_2 reduction with H_2O by deposition of Au CO-catalyst. RSC Adv 7:14186–14191
26. Pandey RR, Alshahrani HS, Krylyuk S, Williams EH, Davydov AV, Chusuei CC (2018) Electrochemical detection of acetaminophen with silicon nanowires. Electroanalysis 30:886–891
27. Sarhangzadeh K (2015) Application of multi wall carbon nanotube–graphene hybrid for voltammetric determination of naproxen. J Iran Chem Soc 12:2133–2140
28. Hegde RN, Hosamani RR, Nandibewoor ST (2009) Electrochemical oxidation and determination of theophylline at a carbon paste electrode using cetyltrimethyl ammonium bromide as enhancing agent. Anal Lett 42:2665–2682
29. Shahrokhian S, Asadian E (2010) Simultaneous voltammetric determination of ascorbic acid, acetaminophen and isoniazid using thionine immobilized multi-walled carbon nanotube modified carbon paste electrode. Electrochim Acta 55:666–672
30. Jiang L, Gu S, Ding Y, Jiang F, Zhang Z (2014) Facile and novel electrochemical preparation of a graphene–transition metal oxide nanocomposite for ultrasensitive electrochemical sensing of acetaminophen and phenacetin. Nanoscale 6:207–214
31. Engin C, Yilmaz S, Saglikoglu G, Yagmur S, Sadikoglu M (2015) Electroanalytical investigation of paracetamol on glassy carbon electrode by voltammetry. Int J Electrochem Sci 10:1916–1925
32. Fan Y, Liu JH, Lu HT, Zhang Q (2011) Electrochemical behavior and voltammetric determination of paracetamol on Nafion/TiO2–graphene modified glassy carbon electrode. Colloids Surf B 85: 289–292
33. Zhang Y, Luo L, Ding Y, Liu X, Qian Z (2010) A highly sensitive method for determination of paracetamol by adsorptive stripping voltammetry using a carbon paste electrode modified with nanogold and glutamic acid. Microchim Acta 171:133–138
34. Adhoum N, Monser L, Toumi M, Boujlel K (2003) Determination of naproxen in pharmaceuticals by differential pulse voltammetry at a platinum electrode. Anal Chim Acta 495:69–75
35. Tashkhourian J, Hemmateenejad B, Beigizadeh H, Hosseini-Sarvari M, Razmi Z (2014) ZnO nanoparticles and multiwalled carbon nanotubes modified carbon paste electrode for determination of naproxen using electrochemical techniques. J Electroanal Chem 714:103–108
36. Baj-Rossi C, Jost TR, Cavallini A, Grassi F, De Micheli G, Carrara S (2014) Continuous monitoring of naproxen by a cytochrome P450-based electrochemical sensor. Biosens Bioelectron 53:283–287
37. Montes RH, Stefano JS, Richter EM, Munoz RA (2014) Exploring multiwalled carbon nanotubes for naproxen detection. Electroanalysis 26:1449–1453
38. Peng A, Yan H, Luo C, Wang G, Ye X, Ding H (2017) Electrochemical determination of theophylline pharmacokinetic under the effect of roxithromycin in rats by the MWNTs/Au/poly-L-lysine modified sensor. Int J Electrochem Sci 12:330–346
39. Zhuang X, Chen D, Wang S, Liu H, Chen L (2017) Manganese dioxide nanosheet-decorated ionic liquid-functionalized graphene for electrochemical theophylline biosensing. Sensors Actuators B Chem 251:185–191
40. da Silva W, Ghica ME, Brett C (2018) Gold nanoparticle decorated multiwalled carbon nanotube modified electrodes for the electrochemical determination of theophylline. Anal Methods 10:5634–5642